Nanoscale

ssDNA-amphiphile architecture used to control dimensions of DNA nanotubes

Journal:	*Nanoscale*
Manuscript ID	NR-ART-05-2019-003761.R1
Article Type:	Paper
Date Submitted by the Author:	30-Jul-2019
Complete List of Authors:	Kuang, Huihui; Johns Hopkins University, Institute for NanoBioTechnology Gartner, Thomas; University of Delaware, Newark, Chemical and Biomolecular Engineering Dorneles de Mello, Matheus; University of Minnesota, Department of Chemical Engineering and Materials Science Guo, Jun; Johns Hopkins University, Institute for NanoBioTechnology Zuo, Xiaobing; Argonne National Laboratory, Tsapatsis, Michael; Johns Hopkins University, Department of Chemical and Biomolecular Engineering, Institute for NanoBioTechnology Jayaraman, Arthi; University of Delaware, Newark, Department of Chemical and Biomolecular Engineering, Department of Materials Science and Engineering Kokkoli, Efrosini; Johns Hopkins University, Department of Chemical and Biomolecular Engineering, Institute for NanoBioTechnology

Nanoscale

ARTICLE

ssDNA-amphiphile architecture used to control dimensions of DNA nanotubes†

Received 00th January 20xx,
Accepted 00th January 20xx

DOI: 10.1039/x0xx00000x

www.rsc.org/

Huihui Kuang,[a] Thomas E. Gartner III,[b] Matheus Dorneles de Mello,[c] Jun Guo,[a] Xiaobing Zuo,[d] Michael Tsapatsis,[a,e] Arthi Jayaraman[b,f] and Efrosini Kokkoli*[a,e]

Controlling the dimensions of DNA nanotubes is of great interest as they can be used in different applications ranging from functional elements in nanodevices to carriers for drug delivery. ssDNA-amphiphiles composed of a ssDNA headgroup, a hydrophobic dialkyl tail and a polycarbon spacer between the tail and the headgroup, self-assemble into hollow DNA nanotubes by forming bilayer nanotapes that transition from twisted nanotapes, to helical nanotapes, to nanotubes. The presence of the DNA nanotubes is verified via cryo-TEM and SAXS. We further explore the effect of the ssDNA secondary structure and tail length on the assembly of the ssDNA-amphiphiles. We demonstrate that the presence of intermolecular G-quadruplexes in the ssDNA sequence dictates the nanotube length. The nanotube diameter is controlled by the hydrophobic tail length, and coarse-grained molecular dynamics simulations are employed to elucidate the tail design impact on assembly.

Introduction

The field of DNA nanotechnology has transformed DNA from a biological material that stores genetic information into a construction material that can be used to build sophisticated 3D scaffolds, structures, and devices with nanoscale features via strategies such as DNA origami,[1] DNA tiles,[2] and DNA bricks.[3] DNA nanotubes have received considerable attention recently due to their applications as templates for nanofabrication[4] and conductive nanowires,[5] selective release of gold nanoparticles,[6] and carriers for drugs and RNA.[7-10] Their application in the delivery of different therapeutics is particularly appealing as DNA nanotubes have encapsulation potential, tunable dimensions, could display targeting ligands or therapeutics on their surface, and have an elongated structure that has been shown to extend the circulation time of polymeric filaments in the body compared to spherical particles.[11] Precise morphological control of DNA nanotubes is an important challenge and currently there are only few examples of controlling their diameter and length. The control over the diameter of the DNA nanotubes can be achieved by programming the circumferences of the tubes by the complementarity of domains in ssDNA,[12] by the directed growth of a sheet of DNA subunits using rolling circle amplification strands as a template,[13] by using hierarchical DNA sub-tiles,[14] and by a set of symmetric star-shaped DNA nanomotifs.[15] Their length can also be controlled using a DNA-templated approach with a DNA guide strand of precise length,[16] or symmetric star-shaped DNA nanomotifs.[15] However, all these approaches require the use of base pairing prediction software and the different DNA segments to be subjected to specific annealing conditions (i.e., controlled cooling rates, specific ions, and pH).

An alternative approach to form DNA nanostructures is to covalently link hydrophilic ssDNA sequences with hydrophobic tails to form ssDNA-amphiphilic molecules.[17, 18] The amphiphilic nature of the conjugates induces their spontaneous assembly in an aqueous environment, with the hydrophobic tails preferring to sequester themselves into a hydrophobic domain while the ssDNA sequences extend into the aqueous solution. With this structural arrangement the ssDNA is not required to base pair to create the nanostructure and remains available for base pairing with complementary ssDNA sequences if needed. Additionally, this approach to forming DNA nanostructures does not require base pairing prediction software and eliminates the requirements for specific annealing conditions.

ssDNA-amphiphiles have been shown to self-assemble into shape-shifting micelles,[19, 20] star-like micelles,[21] and vesicles.[22] We have shown through cryogenic-transmission electron microscopy (cryo-TEM) images that through the inclusion of a polycarbon C_{12} spacer between the ssDNA and a hydrophobic

[a] Institute for NanoBioTechnology, Johns Hopkins University, Baltimore, MD 21218, USA. E-mail: kokkoli@jhu.edu
[b] Department of Chemical and Biomolecular Engineering, University of Delaware, Newark, DE 19716, USA.
[c] Department of Chemical Engineering and Materials Science, University of Minnesota, Minneapolis, MN 55455, USA.
[d] X-Ray Science Division, Argonne National Laboratory, Argonne, IL 60439, USA.
[e] Department of Chemical and Biomolecular Engineering, Johns Hopkins University, Baltimore, MD 21218, USA.
[f] Department of Materials Science and Engineering, University of Delaware, Newark, DE 19716, USA.
†Electronic Supplementary Information (ESI) available.
See DOI: 10.1039/x0xx00000x

C_{16} dialkyl tail, the ssDNA-amphiphiles self-assemble into globular micelles, and bilayer nanotapes that progress to twisted and helical nanotapes, and finally to hollow nanotubes, where the bilayer comprises the wall of the nanotube.[23] Fig. 1 shows a representation of the transitions that lead to the formation of nanotubes as captured by our previous cryo-TEM images.[23] Even though nanotubes have been formed by other amphiphiles, such as peptide-amphiphiles and lipids,[24, 25] our work was the first demonstration that ssDNA-amphiphiles could self-assemble into structures other than cylindrical or spherical micelles. Our work further showed that the inclusion of the polycarbon spacer was important for the formation of the nanotubes as direct conjugation of the ssDNA headgroup to the hydrophobic tail, or use of other spacers only promoted the formation of globular micelles.[22, 26] The bilayer nanotape morphology is not predicted by the standard packing parameter analysis, leading to our hypothesis that polycarbon spacers, through attractive hydrophobic interactions, may force the ssDNA headgroups into close proximity of each other, thus indirectly reducing the interfacial headgroup area and allowing the bilayer nanotapes to form.[26] The twisting of the nanotapes was attributed to the chirality of the ssDNA headgroup.[26] We also demonstrated that the transition from twisted to helical nanotapes occurs as the width of the nanotape increases, showing that the "growing width" model describes the mechanism of transitioning from twisted, to helical nanotapes, to nanotubes.[23] While transition from twisted nanotapes to nanotubes was found to occur over weeks in many other amphiphile systems,[27,28,29] the ssDNA-amphiphiles with the C_{12} polycarbon spacer were observed to form nanotubes soon after dissolution in water, suggesting a possible rapid transition from nanotapes to nanotubes.[23]

The ssDNA-amphiphiles with the C_{12} spacer produced microns long DNA nanotubes with monodispersed diameters of 30 ± 4 nm.[23] In one case only, where a 10 nucleotide (nt) ssDNA sequence was used with five of its ten nucleotides being guanines (G), short nanotubes (60-350 nm in length) were formed.[23] In all instances, ellipsoidal ssDNA micelles (with 9-20 nm ellipsoid axes lengths) were always present and were shown to be the first self-assembled structure after heating and induced disassembly of a sample that contained micelles, nanotapes and nanotubes.[23]

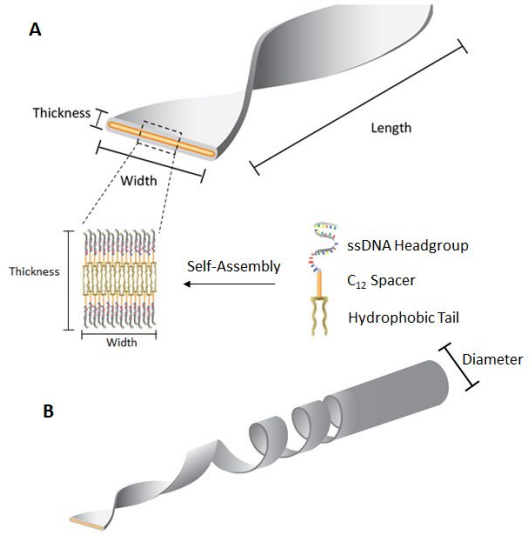

Fig. 1 An artistic representation of (A) the self-assembly of ssDNA-amphiphiles into a bilayer nanotape structure with the thickness, width and length of the nanotape identified, and (B) the self-assembly of the ssDNA nanotubes through the progression of twisted nanotapes, to helical nanotapes, to nanotubes. Adapted from [23] with permission from the Royal Society of Chemistry.

In this report we present a straightforward strategy allowing the design of hollow nanotubes assembled from ssDNA-amphiphiles with controlled diameters and lengths. Building upon our previous finding, we examined the effect of ssDNA guanines on the nanotube length, and show that when they form G-quadruplexes, independent of the sequence length, they can form short tubes with lengths less than 500 nm, and thus present a simple way to control the nanotube length. This is the first demonstration that the DNA secondary structure of ssDNA-amphiphiles, with varying ssDNA lengths, can be used to control the length of nanotubes. We also show that by varying the length of the hydrophobic tail of the ssDNA-amphiphile the diameter of the nanotube can be controlled. This is in contrast to other amphiphiles where, for example, changing the tail length of a peptide-amphiphile mainly resulted in a structural transition.[30-33] To further understand this unexpected result we performed coarse-grained molecular dynamics simulations of bilayers comprised of ssDNA-amphiphiles to demonstrate how the amphiphile design impacts packing at the molecular level within the assembled structures.

Experimental

Materials

Toluene, chloroform ($CHCl_3$), acetone, methanol, tetrahydrofuran (THF), and triethylamine (TEA) were purchased from Fischer Chemical (Hanover Park, IL). ssDNA was purchased from Integrated DNA Technologies (Coralville, IA), cetyl trimethylammonium bromide from Acros Organics (Morris Plains, NJ), and hexafluroisopropanol (HFIP) from Oakwood Products Inc. (West Columbia, SC). Lacey Formvar/carbon 200 mesh copper grids were purchased from Ted Pella Inc. (Redding, CA). SYBR Safe DNA Gel Stain was purchased from Thermo Fisher Scientific (Rockford, IL). All other chemicals and materials were purchased from Sigma-Aldrich (St Louis, MO).

Synthesis of ssDNA-amphiphiles

Dialkyl tails with different lengths (C_{16}, C_{18} or C_{20}) were synthesized as depicted in Fig. S1† and discussed in detail in the ESI.† Products of the synthesis were characterized with ^1H NMR as shown in the ESI.† The ssDNA sequences were purchased with an amino-C_6 linker attached to their 5' end. The ssDNA-amphiphiles were synthesized from a previously published protocol[22] that was modified slightly. 1.5x molar excess cetyl trimethylammonium bromide (CTAB) dissolved in water was added to ssDNA. The NH_4^+ ammonium moiety of

CTAB is electrostatically attracted to the PO_4^- of the ssDNA backbone, forming a sheath of hydrocarbon chains that surround the hydrophilic DNA molecule, which renders the ssDNA soluble in dimethylformamide (DMF). A 10x molar excess of activated tails were added to the CTAB-DNA complexes dissolved in DMF and the reaction was stirred at 50 °C for 24 h. After 24 h, the DMF was removed by evaporation and the ssDNA-amphiphiles and any unreacted ssDNA were purified by lithium perchlorate (2.5% w/v in acetone) precipitation to remove unreacted tails and CTAB. Unreacted ssDNA was separated from the ssDNA-amphiphile using reverse-phase high performance liquid chromatography (RP-HPLC) after they were dissolved in water and filtered through a 0.45 μm polyethersulfone filter. For the RP-HPLC an Agilent Zorbax C3 300 Å SB column was used, with a linear gradient from 5% to 95% buffer B over 25 min at 1 mL/min. Buffer A: 90% water and 10% methanol (v/v), 100 mM HFIP and 14.4 mM TEA. Buffer B: 100% methanol, 100 mM HFIP and 14.4 mM TEA. The molecular weights of the ssDNA-amphiphiles were verified via liquid chromatography-mass spectroscopy (LC/MS) and shown in Table S1.† LC-MS data were acquired with an Agilent Zorbax C8 300 Å SB column with a linear gradient from 50% to 80% buffer B over 30 min at 15 μL/min. Buffer A: 15 mM ammonium acetate in water. Buffer B: Acetonitrile. An Agilent MSD ion trap was used for the determination of the mass.

Cryo-TEM

For cryo-TEM, lacey formvar/carbon 200 mesh copper grids were glow discharged for 60 s to make the grids more hydrophilic. 4 μL of 500 μM ssDNA-amphiphile solutions were deposited onto the grids and vitrified in liquid ethane by Vitrobot (Vitrobot parameters: 5 s blot time, 0 offset, 3 s wait time, 3 s relax time, 95% humidity). After vitrification, the grids were kept under liquid nitrogen and were transferred to a Tecnai G2 Spirit TWIN 20-120 kV/LaB6 TEM operated with an acceleration voltage of 120 kV. Images were captured with an Eagle 2k CCD camera. High resolution cryo-TEM was performed on a FEI Tecnai G2 F30 (S)TEM with TWIN pole piece, a Schottky field-emission electron gun operating at 300 kV and equipped with a Gatan 4k × 4k Ultrascan CCD.

Dynamic light scattering (DLS)

DLS measurements were made using a Nanotrac Flex Analyzer (Microtrac Inc., Montgomeryville, PA). A 200 μM ssDNA-amphiphile solution was heated at 90 °C for 15 min and cooled down to room temperature overnight before measurement. Heating was done to induce disassembly of the amphiphiles and allow for formation of micelles upon cooling.[23]

Small angle x-ray scattering (SAXS)

SAXS experiments were performed at the beamline 12-ID-B of the Advanced Photon Source, Argonne National Laboratory. The data were obtained using a quartz capillary flow cell to minimize beam damage to the sample (200 μM solution of ssDNA-amphiphile in water). The wavelength of X-ray radiation was set to 0.886 Å. Scattered X-ray intensities were measured using a Pilatus 2 M detector. The sample-to-detector distance was set such that the detecting range of momentum transfer q ($q = 4\pi \sin\theta/\lambda$, where 2θ is the scattering angle) was 0.003–0.50 $Å^{-1}$. 40 scattering images were collected for each sample or water to obtain a good signal-to-noise ratio. The 2-D scattering images were converted to 1-D SAXS ($I(q)$ vs. q) curves through azimuthally averaging, using a software package developed for the beamline. The 1D data sets were averaged and subtracted off the water background. The SAXS profiles were fitted using the IRENA package[34]. Details of model fitting and calculations are discussed in ESI.†

Circular dichroism (CD)

ssDNA-amphiphile solutions in water were diluted with Milli-Q water, or different electrolytes and buffers overnight and transferred to a 0.1 cm path length cuvette. The final amphiphile concentration was 20 μM in water, 100 mM KCl, 100 mM NaCl, 5 mM $CaCl_2$, 5 mM $MgCl_2$, 100 mM acetate buffer (pH 5.0), or 100 mM carbonate-bicarbonate buffer (pH 9.0). CD spectra from 320–200 nm were collected using a Jasco J-815 spectrapolarimeter using a read speed of 50 nm/min in 1 nm steps. Three accumulations per amphiphile solution were recorded with the background spectrum automatically subtracted. The accumulations were averaged and the raw ellipticity values were converted to molar ellipticity.

Fluorescence spectra

10 μM ssDNA or ssDNA-amphiphiles in water and 10 μM thioflavin T (ThT) in water were mixed in 96-well microplates (200 μL total volume). Measurements were performed immediately after mixing at room temperature. Fluorescence emission was collected between 460 and 660 nm after excitation at 425 nm in a BioTek Synergy H1 microplate reader (Winooski, VT).

Coarse-grained model

The generic coarse-grained (CG) model used in this work was developed to capture relevant aspects of the ssDNA-amphiphile that dictate self-assembly, including relative hydrophobicity and hydrophilicity, relative stiffness, and relative size of the tail and headgroup regions, as well as the general shape and connectivity of the amphiphile, without treating atomistic chemical details. Five CG bead types were defined to capture the relevant chemical moieties: headgroup (H), amide (A), carboxylate ester (C), tail (T) and water (W). All energy, length, and timescales are reported in the standard Lennard-Jones (LJ) units of ε, σ, and τ. Bonds between CG beads were modelled as harmonic springs with bond constant $K_{bond} = 400\ \varepsilon/\sigma^2$ and equilibrium distance $r_o = \sigma_{ij}$. All non-bonded interactions were modelled with the cut and shifted LJ potential, in which the potential was shifted to zero at $2.5\sigma_{ij}$ (σ_{ij} is the arithmetic mean of the size of beads i and j) for beads exhibiting attractive interactions and $2^{1/6}\sigma_{ij}$ for beads exhibiting purely repulsive interactions (the Weeks-Chandler-Andersen [WCA] potential).[35] The interaction strengths (ε_{ij}) that were chosen to reproduce the amphiphilic self-assembly behaviour of the ssDNA-amphiphiles are shown in Table S2.†

The sizes of A, C, T, and W beads were chosen to be 1.0 σ, and H beads 1.35 σ, representing approximately 0.45 nm and 0.6 nm, respectively.[36, 37] The stiffness of the amphiphile was modelled with a harmonic angle potential with equilibrium angle θ_o = 180 °, angle constant $K_{\theta,H}$ = 3.0 ε/rad^2 for angles defines by H beads, and $K_{\theta,T}$ = 1.0 ε/rad^2 for angles defined by A, C, and T beads.

Simulation method and analysis

Simulations in the NPT ensemble were performed using the LAMMPS MD package.[38] Temperature and pressure were controlled with a Nose-Hoover thermostat and barostat with LAMMPS tdamp and pdamp parameters 0.1 τ and 10.0 τ, respectively. The velocity-Verlet integration algorithm was used, with time-step size *dt* = 0.001 τ. Initial configurations were prepared with the PACKMOL[39] and moltemplate[40] software packages by placing 2,400 amphiphiles in a tail-to-tail bilayer configuration in the *x-y* plane of a periodic 50 σ x 50 σ x 115 σ simulation box. The LAMMPS software was then used to randomly place slabs of 25,000 water beads above and below the bilayer (50,000 water beads total) for simulations containing 10nt headgroups and 62,500 water beads (125,000 water beads total) for simulations containing 25nt headgroups to maintain a consistent hydration level (number of water beads per headgroup bead) between all simulations. Following a short energy minimization to relax overlaps from the random placement of W beads, MD simulations were run with a strong tail-tail attraction of 5 ε for 2 x 10^6 time-steps in the NPT ensemble at *T** = 1.0 and *P** = 0.2, with pressure in the z dimension (normal to the bilayer interface) controlled independently from the x and y dimensions to zero out the interfacial tension of the system. Then the system was run for 1 x 10^6 time-steps in NPT with the x, y, and z dimensions coupled. ε_{TT} was decreased sequentially from ε_{TT} = 4.0 ε, ε_{TT} = 3.0 ε, ε_{TT} = 2.5 ε, ε_{TT} = 2.0 ε every 1 x 10^6 time-steps before reaching the final ε_{TT} of 1.5 ε. The system was advanced another 1 x 10^6 time-steps at *P** = 0.1 with the z dimension controlled independently from the x and y dimensions to re-zero the interfacial tension. Finally, 1 x 10^7 time-steps were completed in the NPT ensemble with isotropic pressure control at *T** = 1.0 and *P** = 0.1 for equilibration and another 1 x 10^7 time-steps for sampling. Snapshots for data collection were saved every 1 x 10^5 time-steps, and 4 independent trials were run for each condition. In order to gauge whether our initial configurations and simulation protocol were affecting our results, we tried multiple bilayer-like initial configurations, including placing the amphiphiles in a tail-to-tail configuration vs. configurations where the amphiphile tails were intercalated. In all cases, the systems relaxed to a tail-to-tail bilayer configuration with dimensions similar to those discussed in the rest of the paper.

The average density profile of all bead types along the *z* dimension (normal to the bilayer) was calculated for each simulation trial. The water-headgroup and headgroup-tail interfaces were defined as the *z*-locations where the density of the headgroup beads was equal to 0.5 times their maximum density. The locations of these interfaces were then used to calculate the bilayer properties such as the total thickness of the bilayer, the thickness of the hydrophobic core, and the density of beads within the hydrophobic core. The area per molecule was calculated as the total *x-y* area of the simulation box divided by 1200 (the number of amphiphiles per layer in the bilayer), and the surface tension was calculated as $\gamma = L_z (P_{zz} - (P_{xx} + P_{yy}) / 2)$, where L_z is the box length in the direction normal to the bilayer, and P_{xx}, P_{yy}, and P_{zz} are the diagonal components of the pressure tensor. Error bars in all simulation results are the standard deviation over the 4 independent trials.

Results and discussion

Synthesis and characterization of ssDNA-amphiphiles

All ssDNA-amphiphiles were synthesized with three building blocks as shown in Fig. 2A: a dialkyl hydrophobic tail with different lengths ($(C_{16})_2$, $(C_{18})_2$, $(C_{20})_2$), a C_{12} hydrophobic polycarbon spacer between the tail and the ssDNA, and a ssDNA hydrophilic headgroup. The ssDNA was purchased with a six-carbon amino linker (C_6 linker) on the 5' end and was conjugated to the C_{12} spacer-tail. In our previous work we showed that ssDNA-amphiphiles with $(C_{16})_2$ tails and a 10nt sequence formed nanotubes in the presence of the C_{12} polycarbon spacer. When the sequence had no G (5'-TTCTATTCTC-3') the tubes were microns long. A G-modified sequence with five consecutive G at the 5' end (5'-GGGGGTTCTC-3'), the point of conjugation to the C_{12} spacer-tail, gave rise to short nanotubes (60-350 nm in length), demonstrating that when 50% of the sequence had G the ssDNA-amphiphiles were self-assembling into short nanotubes. In this work, we investigated the effect of sequence length and number of G required for the formation of short ssDNA nanotubes. Therefore, sequences with approximately 30% G (25ntG_8 and 40ntG_{12}) and 50% G (10ntG_5, 25ntG_{12}) were used as shown in Fig. 2B. Two different versions of the 25ntG_8 sequence were used that could form G-quadruplex, the 25nt-1G_8 with four copies of two contiguous G, and the 25nt-2G_8 that had two copies of three contiguous G and two contiguous G. In addition, we also investigating the effect of tail length on the self-assembly of ssDNA-amphiphiles. The tails and amphiphiles were synthesized as discussed previously,[22, 41] with synthetic details and characterization data provided in ESI, Fig. S1 and Table S1.†

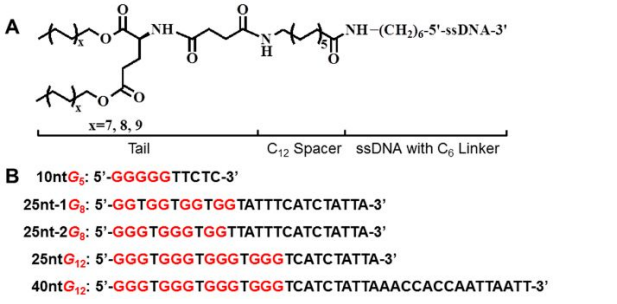

Fig. 2 (A) Chemical structure of ssDNA-amphiphiles. (B) G-rich ssDNA sequences used in this study.

Control of nanotube length self-assembled by G-rich ssDNA-amphiphiles

The morphology of G-rich ssDNA-amphiphiles with $(C_{16})_2$ tails, and different ssDNA lengths bearing different percentages of G was evaluated with cryo-TEM. Previous studies have shown that at low concentrations (below 2.5 μM), G-rich ssDNA sequences form intramolecular (unimolecular) G-quadruplex, whereas at higher concentrations they form intermolecular G-quadruplex.[22] Since all concentrations used in this study are above 2.5 μM, this suggests that the ssDNA-amphiphiles evaluated here form intermolecular G-quadruplexes. Fig. 3 shows micelles and nanotubes formed in water by 25nt-$1G_8$, 25nt-$2G_8$, 25ntG_{12}, and 40ntG_{12} amphiphiles. Spherical micelles are always present, as observed in our previous study.[23] Fig. 4 and Fig. S2† also show cryo-TEMs with larger number of nanotubes. In Fig. 4 the arrows point to nanotubes formed by the 25ntG_{12} amphiphiles that are viewed end-on, demonstrating the hollow nature of these structures, as we have shown previously for the 10ntG_5 amphiphiles.[23] The dark features at the ends of the nanotubes, shown with arrows in Fig. 3, may be attributed to bilayer bulging. Experimental and theoretical studies show that within a fluid bilayer there is molecular reorganization of lipids near the edges of bilayers to minimize the penalty associated with exposing the hydrophobic tails to the water. This reorganization gives rise to dense lipids within a hemi-cylindrical edge that produces a bulging effect on the surrounding bilayer.[42, 43]

The diameters of the micelles were similar to the thickness of the nanotube wall. For example, the 40ntG_{12} amphiphiles formed micelles with a diameter of 8.6 ± 1.2 nm as measured by cryo-TEM and 11.5 ± 1 nm as measured by DLS, and nanotubes with wall thickness of 6 ± 1 nm as measured by cryo-TEM. The difference in micelle diameter between cryo-TEM and DLS is attributed to the fact that electron contrast in TEM derives mostly from the core,[44, 45] while DLS reports the hydrodynamic diameter of the spheres.

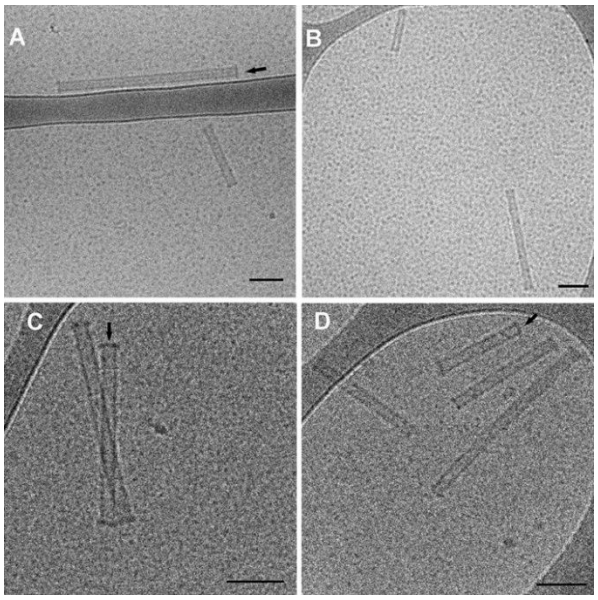

Fig. 3 Cryo-TEM images of spherical micelles and nanotubes formed by (A) 25nt-$1G_8$ amphiphiles, (B) 25nt-$2G_8$ amphiphiles, (C) 25ntG_{12} amphiphiles, and (D) 40ntG_{12} amphiphiles, with $(C_{16})_2$ tails in water. (C) and (D) are high resolution cryo-TEM images. All scale bars are 100 nm.

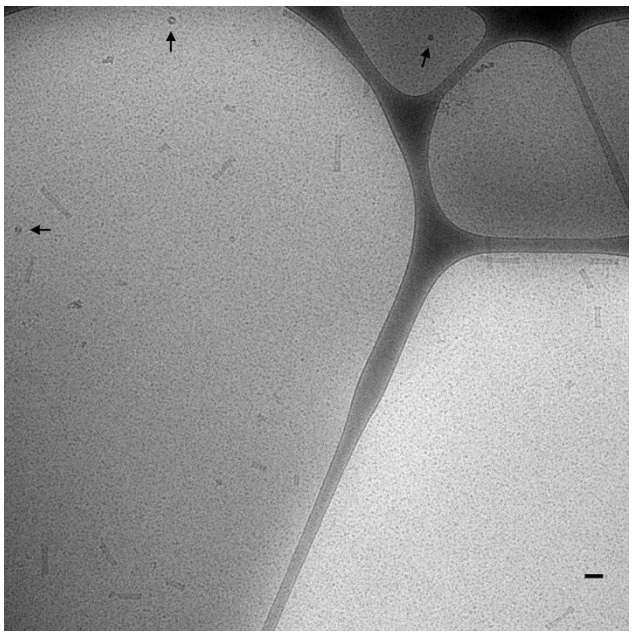

Fig. 4 Cryo-TEM image of spherical micelles and nanotubes formed by 25ntG_{12} amphiphiles with $(C_{16})_2$ tails in water. The black arrows point to nanotubes that are viewed end-on, demonstrating their hollow nature. Scale bar is 100 nm.

SAXS was used in one of the samples to further confirm the coexistence of nanotubes and micelles as it was done before to support the presence of nanotapes formed by our ssDNA-amphiphiles.[26] Specifically, the 40ntG_{12} sequence, free and as an amphiphile with $(C_{16})_2$ tail were evaluated with SAXS and results are shown in Fig. 5. The experimental data showed a feature at q around 0.15 - 0.2 A^{-1}, attributed to scattering from the ssDNA corona (Fig. 5A). The scattering from free ssDNA was then subtracted from the experimental data and the remaining scattering was attributed to the hydrophobic core of the tubes and micelles. A model considering only scattering from spherical micelles fitted the data well at the high q region ($q > 0.014$ A^{-1}). Specifically, to capture the chemical structure of the hydrophobic portion of the amphiphile, a core-multishell sphere model with two shells (Fig. 5B) was used to describe the structure of the micelles and the corresponding contributions of the components to the scattering. Table S3† gives the calculated scattering length densities of the core-multishell model. At low q values, there is scattering intensity which cannot be accounted for by the spherical micelle model (Fig. 5C). Therefore, this scattering is attributed to another type of particle which based on the cryo-TEM data should be the nanotubes. Indeed, the power law of the form $I(q) \sim q^{-1}$ at low q values ($q < 0.01$ A^{-1}) is indicative of cylindrical objects in solution which can be described adequately by a core-shell cylinder model (Fig. 5B). Addition of the sphere and cylinder models provided a good fit over the entire q range (Fig. 5C). Although it is expected that the shell of the cylinder should have a similar structure as the micelle shell, we did not use a core-two shell cylinder model because of software limitations.

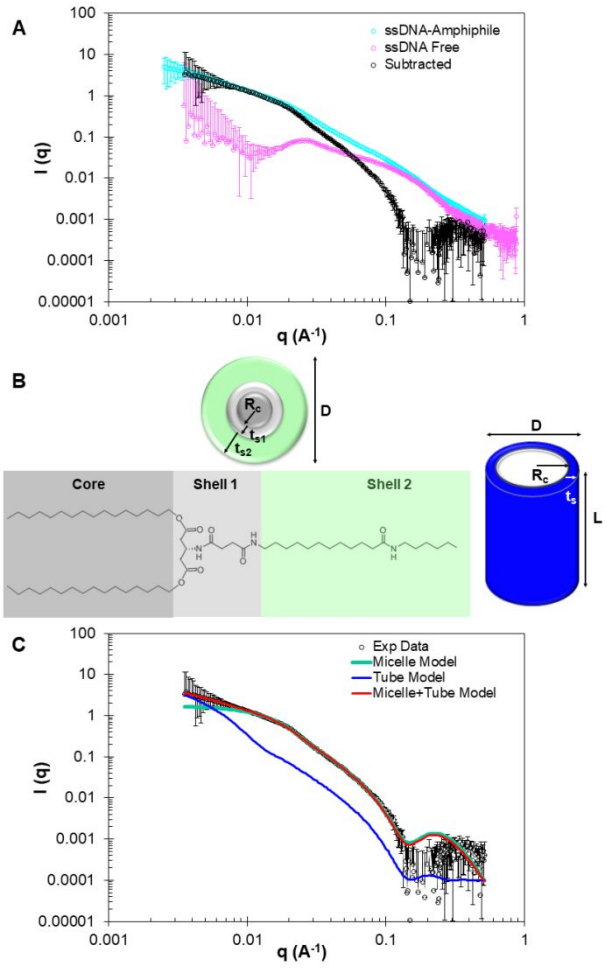

Fig. 5 (A) Core-two shell sphere model and core-shell cylinder model used for the fitting of the SAXS data. (B) SAXS data for the 40ntG$_{12}$ amphiphiles with $(C_{16})_2$ tails in water and the fit to the data.

However, we do not expect significant changes by using a more detailed model for the nanotubes, because its effect on the scattering would be manifested in the high q region which is dominated by features of similar size (wall thickness of the tubes and diameter of the micelles) that are common to micelles and tubes. We note that the micelle and cylinder models did not consider any contribution from structure factor, assuming that the solution is dilute enough. Table S4† gives the scattering length densities calculated for the core-shell cylinder model. The results of the fitting are shown in Fig. 5C and Table 1. The micelle diameter obtained from SAXS fitting (5.9 ± 1.1 nm) is similar to the one measured by cryo-TEM (8.6 ± 1.2 nm) and smaller than the one measured by DLS (11.5 ± 1 nm), which is expected because the subtracted SAXS data do not consider the contribution of ssDNA to the object size. The nanotube dimensions obtained from SAXS (wall thickness of 4.3 ± 0.7 nm, diameter 25.0 ± 3.0 nm, and length of 220 ± 150 nm) are also similar to the ones measured by cryo-TEM (wall thickness of 6 ± 1 nm, diameter 29 ± 2 nm, and length of 233 ± 116 nm).

Table 1 Fitted parameters of SAXS data for 40ntG$_{12}$ amphiphiles with $(C_{16})_2$ tails

Micelles		Nanotubes	
R_c (nm)	1.2 ± 0.6	R_c (nm)	8.3 ± 2.3
t_{s1} (nm)	0.7 ± 0.02	t_s(nm)	4.3 ± 0.7
t_{s2} (nm)	1.1 ± 0.5	L (nm)	220 ± 150
ρ_{s1} (x10^{10} cm^{-2})[a]	11.8 ± 0.3	ρ_s (10^{10} cm^{-2})[a]	13.69 ± 0.4
D (nm)	5.9 ± 1.1	D (nm)	25.0 ± 3.0

[a]ρ_{s1} and ρ_s are the scattering length densities of micelle shell 1 and cylinder shell respectively.

Diameters and lengths of nanotubes formed by all ssDNA-amphiphiles, measured by cryo-TEM, are shown in Table 2. One of the drawbacks of cryo-TEM is that most of the sample volume is lost during the blotting step,[46] and for samples where nanotubes are observed less frequently, a large number of measurements may not be feasible. To examine if a smaller sample could be used, 20 measurements were randomly chosen from each of these 100 nanotubes. T-test analysis showed that there was no statistically significant difference ($p > 0.05$) between groups with 20 and 100 measurements for either the diameter or length. Therefore, 20 cryo-TEM nanotube measurements were collected in the rest of the paper. As shown in Table 2, all G-rich sequences with $(C_{16})_2$ tails formed short nanotubes with monodispersed diameters of about 30 nm and submicron lengths. In contrast, ssDNA-amphiphiles with 10nt, 25nt and 40nt long ssDNA headgroups with no G, self-assembled into microns long nanotubes.[23] Comparison of the diameters of the G-rich amphiphiles with $(C_{16})_2$ tails showed that there was no statistically significant difference for all pairs ($p > 0.05$). The results of the statistical analysis for length comparisons are shown in Table S5† and show no correlation between the number of G in the ssDNA sequence and nanotube length.

Our previous work showed that the "growing width" model described the mechanism of transitioning from twisted nanotapes, to helical nanotapes, to nanotubes, and that after disassembly of all formed nanostructures (spherical micelles, nanotapes and nanotubes) the first re-assembled structure was the globular micelles.[23] Therefore, the micelles have to release the amphiphiles that can attach to the nanotapes and allow for the nanotape growth. It has also been shown that

Table 2 Diameter and length of nanotubes in water formed by G-rich ssDNA-amphiphiles with $(C_{16})_2$ tails[a,b]

ssDNA-Amphiphiles	Diameter (nm) (n=100)	Diameter (nm) (n=20)	Length (nm) (n=100)	Length (nm) (n=20)
10ntG$_5$	29 ± 2	29 ± 2	306 ± 165	272 ± 135
25nt-1G$_8$	30 ± 2	29 ± 2	270 ± 165	274 ± 129
25nt-2G$_8$	29 ± 2	29 ± 2	347 ± 163	286 ± 119
25ntG$_{12}$	30 ± 2	30 ± 2	148 ± 67	167 ± 67
40ntG$_{12}$	29 ± 2	29 ± 1	233 ± 116	210 ± 88

[a]Measurements are from cryo-TEM images; data are presented as mean ± SD. [b]t-Test statistical analysis comparing diameter or length for each amphiphile between n=100 and n=20 groups gave p>0.05 for all samples; one-way ANOVA with Tukey's HSD post-hoc analysis showed no statistically significant difference (p>0.05) for all diameter pairs (n=100 or n=20), p-values from length comparisons between different amphiphiles are reported in Table S5.†

micelles assembled from ssDNA-amphiphiles that form intermolecular parallel G-quadruplexes in the micelles are more stable, as removal of these amphiphiles from the micelles is more difficult compared to amphiphiles that do not form intermolecular G-quadruplexes.[47] Therefore, we hypothesize that in the presence of G where ssDNA headgroups can form intermolecular stacked G-tetrad planes in the micelle, the self-assembled micelles are more stable resulting in amphiphiles that are less prone to leaving the micelles and assembling in the nanotapes, thus resulting in shorter nanotubes.

The secondary structure of the ssDNA-amphiphiles and presence of G-quadruplexes was investigated by CD. Parallel-stranded G-quadruplex structures have a CD spectrum exhibiting a strong positive peak at 260–265 nm and a smaller negative peak around 245 nm.[48, 49] They are stabilized by small cations that fit within the G-quartet structure but can also be formed in pure water.[23, 50] The CD spectra of the amphiphiles with the $(C_{16})_2$ tails are shown in Fig. 6. The 25ntG_{12} and 40ntG_{12} amphiphiles have a maximum at 263 and 265 nm respectively, whereas the 25nt-1G_8 and 25nt-2G_8 amphiphiles have a maximum at 268 and 269 nm respectively. All amphiphiles have a minimum at 242-245 nm. Therefore, the 25ntG_{12} and 40ntG_{12} amphiphiles have a spectrum that is characteristic of G-quadruplex structure. To investigate further the secondary structure of the amphiphiles, thioflavin T (ThT) was used as a fluorescence probe to detect G-quadruplex formation. ThT has been used in the literature to discriminate G-quadruplex and GA-containing non-G-quadruplex formation from duplexes and single strands.[51-53] In particular, it was shown that a 60-fold increase in the fluorescence of ThT could be observed in the presence of a ssDNA sequence that forms G-quadruplex.[52] Fig. 7A shows the emission spectra of ThT in the absence (FIo) and presence of ssDNA or ssDNA-amphiphiles (FI). All sequences examined induced a significant increase in ThT fluorescence, FI/FIo, (Fig. 7B), with the ssDNA-amphiphiles having a more pronounced effect than ssDNA, suggesting that there are G-quadruplex interactions between all the amphiphile headgroups following self-assembly. Interestingly, the 25ntG_{12} and 40ntG_{12} amphiphiles gave the highest enhancement of the fluorescence of ThT, confirming the presence of strong G-quadruplexes in agreement with the CD data. Taken together, our data demonstrate that ssDNA-amphiphiles with a ssDNA sequence of varying length and G content that can form parallel G-quadruplexes with neighbouring amphiphiles, self-assemble into short nanotubes. Our previous work has shown that 10nt, 25nt and 40nt long ssDNA with no G, self-assembled into microns long nanotubes when conjugated to C_{12} spacer-$(C_{16})_2$ tails, like the ones used in this study.[23]

Previous work on nanotubes formed by self-assembly of amphiphilic molecules has demonstrated limited control over nanotube length. Examples include controlling the length from a few microns to hundreds of microns by changing the solvent using different mixtures of alcohol-water,[54, 55] or varying the length from 1-100 µm by decreasing the cooling rate through the gel-to-liquid crystalline phase transition temperature in an ethanol-water mixture.[56] Mechanical stirring has also been used to produce nanotubes with 600-800 nm lengths.[57] However none of these approaches could produce short nanotubes (with lengths less than 500 nm), and the need of different solvents may limit their application. Our study shows the advantage of using ssDNA-amphiphiles to form nanotubes, as by having a G-rich sequence of varying length that can form G-quadruplexes, one can produce short nanotubes.

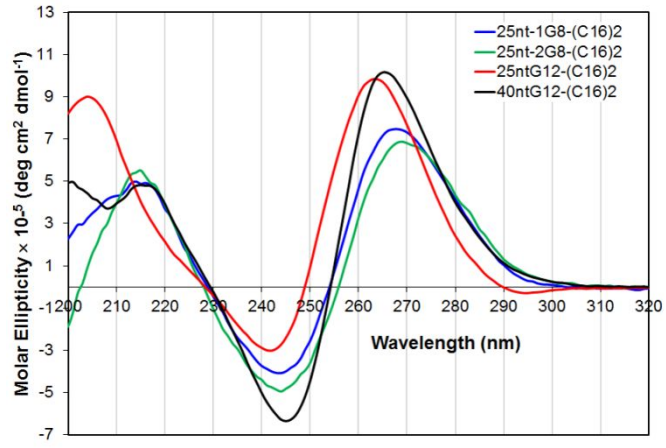

Fig. 6 CD spectra in water of G-rich ssDNA-amphiphiles with $(C_{16})_2$ tails.

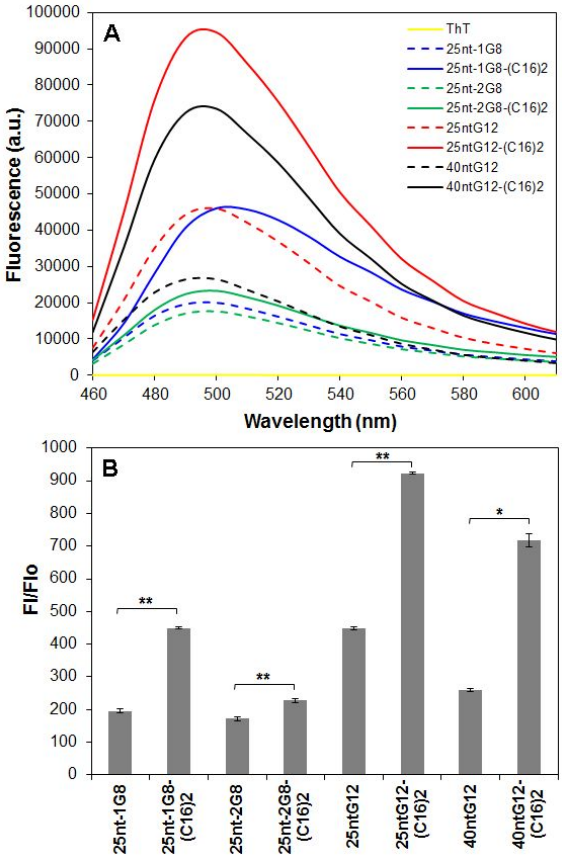

Fig. 7 (A) Fluorescence emission spectra of ThT in the presence of ssDNA or ssDNA-amphiphiles with $(C_{16})_2$ tails. (B) Fluorescence intensity enhancement (FI/FIo) of ThT at 500 nm in the presence of ssDNA or ssDNA-amphiphiles with $(C_{16})_2$ tails. Data are presented as mean ± SD (n=3). t-Test statistical analysis, **p<0.001, *p<0.05.

Stability of nanotubes formed by G-rich ssDNA-amphiphiles in different electrolytes and pH

Short ssDNA nanotubes may find different applications that need the presence of electrolytes or different pH conditions. Therefore, the stability of short nanotubes in the presence of different electrolytes and pH was investigated. Solutions of 25ntG_{12} amphiphiles with $(C_{16})_2$ tails in water were diluted with different electrolytes (100 mM KCl, 100 mM NaCl, 5 mM $CaCl_2$, 5 mM $MgCl_2$) or buffers (100 mM acetate buffer pH 5.0, 100 mM carbonate-bicarbonate buffer pH 9.0) overnight and evaluated with cryo-TEM and CD. Cryo-TEM images (Fig. S3†) showed that the presence of different electrolytes or pH did not change the shape or dimensions of the short nanotubes, as their diameter and length were similar to the ones observed in water (Table 3). Their CD spectra (Fig. S4†) in different electrolytes and pH exhibited a strong positive peak at 263-264 nm and a smaller negative peak at 241-242 nm, characteristic of G-quadruplex structure as shown in water (Fig. 6). Hence, these data suggest that the short nanotubes formed by G-rich ssDNA-amphiphiles are stable in different electrolytes and pH.

Effect of tail length on the diameter of ssDNA-amphiphile nanotubes

Diameter control of lipid nanotubes from 80 ± 20 to 960 ± 120 nm has been achieved by modifying the lipid headgroup size, pH and solvent ionic strength.[24] Binary lipid mixtures allowed for tuning of nanotube diameter from 79 ± 8 to 127 ± 12 nm,[58] or from 500 nm to 45-55 nm.[59] The molecular length of unsymmetrical (wedge-shaped) boloamphiphiles has also been used to control the lipid nanotube diameter.[60] In all of these cases the nanotubes were microns long.

In this study we conjugated the ssDNA sequences shown in Fig. 2B to $(C_{18})_2$ and $(C_{20})_2$ tails, in addition to $(C_{16})_2$ tails, and evaluated their self-assembly in water with CD and cryo-TEM. CD spectra for the G-rich amphiphiles with $(C_{18})_2$ and $(C_{20})_2$ tails (Fig. S5†) were similar to the ones observed for the ssDNA-amphiphiles with $(C_{16})_2$ tails (Fig. 6). Fig. 8A,B shows the effect of tail length on the width of twisted nanotapes formed by 40ntG_{12} amphiphiles. As the tail length increased from $(C_{18})_2$ to $(C_{20})_2$ the width of the twisted nanotapes captured in these images changed from 39 ± 2 nm to 50 ± 2 nm respectively. As the tail length increased, the nanotube diameter increased as well as shown in Fig. 8C,D for the 40ntG_{12} amphiphiles. Fig. S6† also shows nanotubes and spherical micelles assembled from the 10ntG_5 amphiphiles with $(C_{18})_2$ and $(C_{20})_2$ tails, and Table 4 gives nanotube diameters and lengths for all amphiphiles examined with $(C_{18})_2$ and $(C_{20})_2$ tails. As the tail length increases from $(C_{16})_2$ to $(C_{20})_2$, the diameter of the nanotubes increases from approximately 29 nm to 54 nm, and nanotubes are observed less frequently.

An increase in the tail length did not have an effect on the nanotube length for most sequences. With respect to the effect of G-rich sequences on the nanotube length when longer tails were used, similar to the $(C_{16})_2$ tails, short submicron nanotubes were observed. In contrast, Fig. S7A† shows a micron long nanotube assembled from a 10nt sequence with no G conjugated to a $(C_{18})_2$ tail, and for comparison a micron long nanotube assembled from the same sequence with a $(C_{16})_2$ tail is also shown (Fig. S7B†). The effect of tail length on sequences of different lengths with no G is outside the scope of this work and was not examined further.

Table 3 Diameter and length of nanotubes formed by 25ntG_{12} amphiphiles with $(C_{16})_2$ tails in different conditions[a,b]

Solution	Diameter (nm)	Length (nm)
water	30 ± 2	167 ± 67
100 mM KCl	29 ± 2	156 ± 51
100 mM NaCl	30 ± 2	137 ± 52
5 mM CaCl2	30 ± 2	133 ± 64
5 mM MgCl2	29 ± 2	163 ± 56
pH 5	29 ± 2	170 ± 77
pH 9	29 ± 2	145 ± 61

[a]ssDNA-amphiphile solutions in water were diluted with different electrolytes or buffers overnight; measurements are from cryo-TEM images (n=20); water measurements from Table 1 are included for comparison; data are presented as mean ± SD. [b]One-way ANOVA showed no statistically significant difference for all diameter or length pairs (p>0.1).

Coarse-grained molecular dynamics (CGMD) simulations of ssDNA-amphiphile bilayers

To investigate the effect of tail length on the self-assembly of ssDNA-amphiphiles and how the amphiphile design impacts packing at the molecular level within the assembled structures, CGMD simulations of bilayers comprised of ssDNA-amphiphiles were performed. With modest computational resources, we chose to simulate the bilayer configuration in the simulation box as it represents a small (locally flat) region in the plane of the bilayer nanotape, which subsequently folds/bends to create twisted and helical nanotapes that

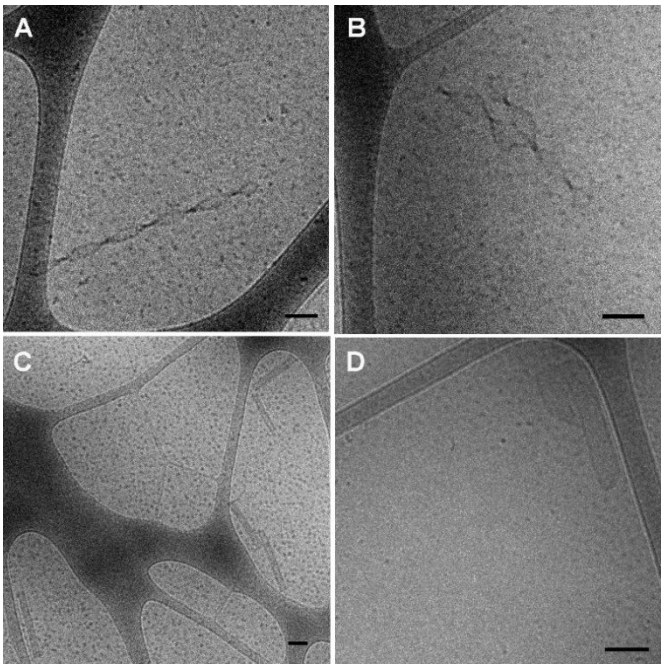

Fig. 8 Cryo-TEM images of 40ntG_{12} amphiphiles with $(C_{18})_2$ tails forming (A) twisted nanotapes and (C) nanotubes, and with $(C_{20})_2$ tails forming (B) twisted nanotapes and (D) nanotubes. Spherical micelles are present in all images. Scale bars are 100 nm.

Table 4 Diameter and length of nanotubes formed by G-rich ssDNA-amphiphiles with $(C_{18})_2$ and $(C_{20})_2$ tails in water[a,b]

ssDNA-Amphiphiles	Diameter (nm)	Length (nm)
10ntG_5-$(C_{18})_2$	40 ± 3	218 ± 124
10ntG_5-$(C_{20})_2$	53 ± 5	165 ± 76
25nt-1G_8-$(C_{18})_2$	39 ± 2	207 ± 106
25nt-1G_8-$(C_{20})_2$	55 ± 4	162 ± 67
25nt-2G_8-$(C_{18})_2$	39 ± 3	282 ± 137
25nt-2G_8-$(C_{20})_2$	52 ± 6	195 ± 148
25ntG_{12}-$(C_{18})_2$	39 ± 2	177 ± 84
25ntG_{12}-$(C_{20})_2$	53 ± 5	180 ± 101
40ntG_{12}-$(C_{18})_2$	38 ± 2	318 ± 82
40ntG_{12}-$(C_{20})_2$	56 ± 5	308 ± 165

[a]Measurements are from cryo-TEM images (n=20); data are presented as mean ± SD; nanotubes were observed infrequently for the $(C_{20})_2$ tails. [b]One-way ANOVA with post-hoc Tukey's HSD test analysis comparing nanotube diameters of amphiphiles with $(C_{16})_2$-$(C_{20})_2$ tails for each sequence gave $p<0.001$ for all diameter pairs; p-values from length comparisons are reported in Table S6†; no statistically significant difference observed ($p>0.05$) for all $(C_{18})_2$ or $(C_{20})_2$ diameter pairs; p-values from length comparisons between different amphiphiles with $(C_{18})_2$ or $(C_{20})_2$ tails are reported in Table S7† and S8† respectively.

progress into nanotubes as discussed above and shown in Fig. 1. We note that there are many past simulation studies, atomistic as well as coarse-grained, that have focused on assembly of DNA functionalized nanoparticles and assembly for DNA origami.[61, 62] There is also some past work using atomistic and CG simulations aimed at assembly of peptide-amphiphiles.[63, 64] In this work, we chose to use a more generic CG model inspired by past CG models of lipid bilayer assembly in order to study the key physical implications of changing amphiphile design.[36, 65-73] The mapping of CG beads onto the chemical structure of a ssDNA-amphiphile is shown in Fig. 9A. This generic CG model allowed us to focus on the impact of molecular design and architecture on self-assembly over nanometer length scales with modest computational resources. One could use a back-mapping scheme to incorporate finer-scale chemical details into the results of these CGMD simulations; this approach is outside the scope of this work. We discuss some of these important considerations in CG model development, and their relative advantages and disadvantages, in a perspective article on macromolecular simulations.[74]

Four representative systems were modelled to understand the impact of tail length and headgroup length on ssDNA-amphiphile self-assembly: 10nt headgroup with $(C_{16})_2$ tails (10nt-$(C_{16})_2$), 10nt headgroup with $(C_{20})_2$ tails (10nt-$(C_{20})_2$), 25nt headgroup with $(C_{16})_2$ tails (25nt-$(C_{16})_2$), and 25nt headgroup with $(C_{20})_2$ tails (25nt-$(C_{20})_2$). The number of water beads included in the simulations was adjusted such that the headgroup hydration level (number of water beads per headgroup bead) was consistent between the $(C_{16})_2$ and $(C_{20})_2$ simulations. All systems explored formed a stable bilayer with no pores, as shown by representative simulation snapshots in Fig. 9B,C. Independent translation of amphiphiles within the plane of the bilayer (i.e., bilayer fluidity) was confirmed via visual inspection of the simulation trajectory using the Visual Molecular Dynamics (VMD) software.[75] The density profiles in the direction normal to the bilayer (z) for the four simulated systems are plotted in Fig. 9D for the 10nt-$(C_{16})_2$ amphiphiles and Fig. S8† for the rest of the amphiphiles. All systems exhibited qualitatively similar density distributions, with strong

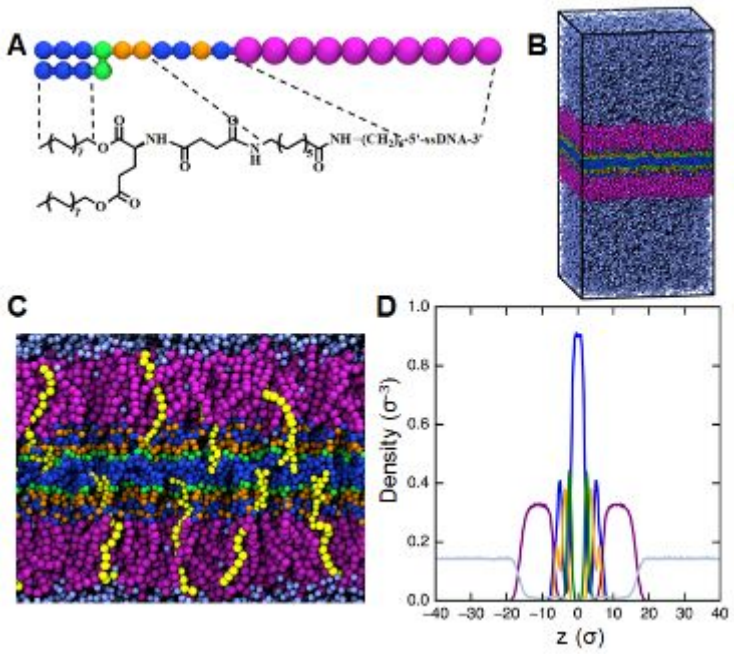

Fig. 9 (A) Mapping of CGMD simulation beads to the 10nt-$(C_{16})_2$ amphiphile chemical structure. T beads (blue) represent ~5 carbons of an alkyl chain, C beads (green) represent a carboxylate ester group and one additional carbon, A beads (orange) represent an amide group and one additional carbon, and H beads (purple) represent a single ssDNA nucleotide. (B) Simulation snapshot of bilayer formed by 10nt-$(C_{16})_2$ amphiphiles. (C) Zoomed-in snapshot of a 10nt-$(C_{16})_2$ amphiphile bilayer, with selected amphiphiles rendered in yellow to demonstrate how individual molecules pack in the bilayer. Light blue beads in (B,C) represent the water W. (D) Number density of various CG beads of 10nt-$(C_{16})_2$ amphiphiles as a function of position normal to the bilayer (z) for bead types T (blue), C (green), A (orange), H (purple), and W (light blue). σ is the standard LJ reduced distance unit.

Table 5 Summary of bilayer structural properties from CGMD simulations[a]

ssDNA-Amphiphiles	Total bilayer thickness[b] (σ)	Hydrophobic layer thickness[b] (σ)	Hydrophobic layer density[b] (σ^{-3})	Area per molecule[b] (σ^2)	Surface tension, $\gamma^{b,c}$ (ε/σ^2)
10nt-$(C_{16})_2$	32.48 ± 0.11	13.87 ± 0.07	0.618 ± 0.001	3.318 ± 0.011	0.74 ± 0.05
10nt-$(C_{20})_2$	32.53 ± 0.17	14.67 ± 0.07	0.640 ± 0.002	3.462 ± 0.017	0.89 ± 0.05
25nt-$(C_{16})_2$	59.00 ± 0.88	13.80 ± 0.13	0.610 ± 0.004	3.393 ± 0.058	-0.17 ± 0.25
25nt-$(C_{20})_2$	57.33 ± 0.07	14.40 ± 0.07	0.631 ± 0.001	3.589 ± 0.002	0.24 ± 0.04

[a]Data presented as mean ± SD. [b]σ is the standard LJ reduced distance unit. [c]ε is the standard LJ reduced energy unit.

segregation between the hydrophilic (purple) and hydrophobic (orange, green, blue) regions. A small fraction of water beads penetrated into the headgroup region of the bilayer (Fig. 9C), but no water was present in the dialkyl tail region (near z = 0).

A quantitative analysis of how amphiphile design affected the bilayer structure is provided in Table 5. First, for the same tail length, increasing the ssDNA length from 10nt to 25nt increased the total bilayer thickness to accommodate the additional headgroup beads. Also, increasing the headgroup length slightly increased the area per molecule and decreased the bilayer surface tension, likely due to the increased number of headgroup beads which are strongly attracted to the water. We note that the numerical value of the bilayer surface tension obtained from simulations can depend on many factors, including the details of the molecular model employed, the system size (i.e., number of amphiphilic molecules), the simulation ensemble (e.g., constant volume vs. constant pressure vs. constant surface area).[76] Thus, we emphasize the trend in surface tension as a function of amphiphile design, rather than the precise numerical values. Considering a change in tail length for the same headgroup, the total thickness of the bilayer did not appreciably change as the tail length increased from C_{16} to C_{20}. In contrast, the hydrophobic layer thickness and density as well as the area per molecule increased as the tail length increased.

In addition to providing a mapping between ssDNA-amphiphile design and bilayer properties, these simulations reveal two key phenomena which could explain the experimental trends in nanotube diameter discussed above. First, the increase in area per molecule within the bilayer as tail length increases could result in an increase in nanotape width as shown in Fig. 8A,B. Wider nanotapes will therefore transition into nanotubes with larger diameters (Fig. 8C,D). Secondly, with longer tails the resulting thicker and more dense hydrophobic layer increases the bilayer bending modulus and resistance to the formation of curved interfaces,[77, 78] resulting in bilayers with lower curvature (e.g., larger nanotube diameter). This increased resistance to curvature with longer tails may also explain the experimental observation that nanotubes were less abundant for the $(C_{20})_2$ tails.

Conclusions

To realize the full potential of DNA nanotubes in a variety of applications, there is a need to develop simple, robust, and cost-effective strategies for their assembly with defined geometry (both length and diameter). This is the first demonstration that the secondary structure of the ssDNA can be used to control the length of DNA nanotubes self-assembled from ssDNA-amphiphiles, and that the tail of the amphiphile influences the diameter of the nanotube. In particular, G-rich ssDNA-amphiphiles with different ssDNA lengths and G percentages, forming parallel G-quadruplexes with neighboring amphiphiles, can self-assemble into short nanotubes that are stable in water and different electrolytes. In contrast, ssDNA with no G self-assemble only into microns long nanotubes. Increasing the length of the hydrophobic tail from $(C_{16})_2$ to $(C_{20})_2$ resulted in wider nanotapes and nanotubes due to increasing the area per molecule in the bilayer and a thicker hydrophobic layer resisting curvature as demonstrated by CGMD simulations.

Conflicts of interest

There are no conflicts to declare.

Acknowledgements

This work was supported in part by UMN's MnDRIVE and the National Science Foundation (NSF DMR-1609543). This research used resources of the Advanced Photon Source, a U.S. Department of Energy (DOE) Office of Science User Facility operated for the DOE Office of Science by Argonne National Laboratory under Contract No. DE-AC02-06CH11357. The simulations were conducted through the use of Information Technologies (IT) resources at the University of Delaware, specifically the high-performance computing resources of the Farber supercomputing cluster.

Notes and references

1 D. Han, S. Pal, J. Nangreave, Z. Deng, Y. Liu and H. Yan, *Science*, 2011, **332**, 342-346.

2 B. Wei, M. Dai and P. Yin, *Nature*, 2012, **485**, 623-626.

3 Y. Ke, L. L. Ong, W. M. Shih and P. Yin, *Science*, 2012, **338**, 1177-1183.
4 C. Lin, Y. Ke, Y. Liu, M. Mertig, J. Gu and H. Yan, *Angewandte Chemie-International Edition*, 2007, **46**, 6089-6092.
5 D. Liu, S. H. Park, J. H. Reif and T. H. LaBean, *Proc. Natl. Acad. Sci. U. S. A.*, 2004, **101**, 717-722.
6 P. K. Lo, P. Karam, F. A. Aldaye, C. K. McLaughlin, G. D. Hamblin, G. Cosa and H. F. Sleiman, *Nat. Chem.*, 2010, **2**, 319-328.
7 S. Sellner, S. Kocabey, T. Zhang, K. Nekolla, S. Hutten, F. Krombach, T. Liedl and M. Rehberg, *Biomaterials*, 2017, **134**, 78-90.
8 S. Ko, H. Liu, Y. Chen and C. Mao, *Biomacromolecules*, 2008, **9**, 3039-3043.
9 Z. You, H. Qian, C. Wang, B. He, J. Yan, C. Mao and G. Wang, *Biomaterials*, 2015, **67**, 137-150.
10 Q. Liu, D. Wang, M. Yuan, B. F. He, J. Li, C. Mao, G. S. Wang and H. Qian, *Chem. Sci.*, 2018, **9**, 7562–7568.
11 Y. Geng, P. Dalhaimer, S. Cai, R. Tsai, M. Tewari, T. Minko and D. E. Discher, *Nature Nanotechnology*, 2007, **2**, 249-255.
12 P. Yin, R. F. Hariadi, S. Sahu, H. M. T. Choi, S. H. Park, T. H. LaBean and J. H. Reif, *Science*, 2008, **321**, 824-826.
13 O. I. Wilner, R. Orbach, A. Henning, C. Teller, O. Yehezkeli, M. Mertig, D. Harries and I. Willner, *Nat. Commun.*, 2011, **2**, 540.
14 X. Shi, X. Wu, T. Song and X. Li, *Nanoscale*, 2016, **8**, 14785-14792.
15 H. Qian, C. Tian, J. Yu, F. Guo, M.-S. Zheng, W. Jiang, Q.-F. Dong and C. Mao, *Small*, 2014, **10**, 855-858.
16 P. K. Lo, F. Altvater and H. F. Sleiman, *J. Am. Chem. Soc.*, 2010, **132**, 10212-10214.
17 M. Kwak and A. Herrmann, *Chem. Soc. Rev.*, 2011, **40**, 5745-5755.
18 A. Patwa, A. Gissot, I. Bestel and P. Barthelemy, *Chem. Soc. Rev.*, 2011, **40**, 5844-5854.
19 M.-P. Chien, A. M. Rush, M. P. Thompson and N. C. Gianneschi, *Angew. Chem. Int. Ed.*, 2010, **49**, 5076-5080.
20 Z. Zhao, L. Wang, Y. Liu, Z. Yang, Y.-M. He, Z. Li, Q.-H. Fan and D. Liu, *Chem. Commun.*, 2012, **48**, 9753-9755.
21 L. Tang, V. Tjong, N. Li, Y. G. Yingling, A. Chilkoti and S. Zauscher, *Adv. Mater.*, 2014, **26**, 3050-3054.
22 B. Waybrant, T. R. Pearce and E. Kokkoli, *Langmuir*, 2014, **30**, 7465-7474.
23 T. R. Pearce and E. Kokkoli, *Soft Matter*, 2015, **11**, 109-117.
24 T. Shimizu, M. Masuda and H. Minamikawa, *Chem. Rev.*, 2005, **105**, 1401-1444.
25 T. Shimizu, H. Minamikawa, M. Kogiso, M. Aoyagi, N. Kameta, W. Ding and M. Masuda, *Polym. J.*, 2014, **46**, 831-858.
26 T. R. Pearce, B. Waybrant and E. Kokkoli, *Chem. Commun.*, 2014, **50**, 210-212.
27 E. T. Pashuck and S. I. Stupp, *J. Am. Chem. Soc.*, 2010, **132**, 8819-8821.
28 L. Ziserman, H.-Y. Lee, S. R. Raghavan, A. Mor and D. Danino, *J. Am. Chem. Soc.*, 2011, **133**, 2511-2517.
29 J. Adamcik, V. Castelletto, S. Bolisetty, I. W. Hamley and R. Mezzenga, *Angew. Chem. Int. Ed.*, 2011, **50**, 5495-5498.
30 S. Santoso, W. Hwang, H. Hartman and S. G. Zhang, *Nano Lett.*, 2002, **2**, 687-691.
31 H. Xu, J. Wang, S. Han, J. Wang, D. Yu, H. Zhang, D. Xia, X. Zhao, T. A. Waigh and J. R. Lu, *Langmuir*, 2009, **25**, 4115-4123.
32 S. Bucak, C. Cenker, I. Nasir, U. Olsson and M. Zackrisson, *Langmuir*, 2009, **25**, 4262-4265.
33 T. Gore, Y. Dori, Y. Talmon, M. Tirrell and H. Bianco-Peled, *Langmuir*, 2001, **17**, 5352-5360.
34 J. Ilavsky and P. R. Jemian, *J. Appl. Crystallogr.*, 2009, **42**, 347-353.
35 D. Chandler and J. D. Weeks, *Phys. Rev. Lett.*, 1970, **25**, 149-&.
36 S. J. Marrink, A. H. de Vries and A. E. Mark, *J. Phys. Chem. B*, 2004, **108**, 750-760.
37 A. F. Ghobadi and A. Jayaraman, *Soft Matter*, 2016, **12**, 2276-2287.
38 S. Plimpton, *J. Comput. Phys.*, 1995, **117**, 1-19.
39 L. Martinez, R. Andrade, E. G. Birgin and J. M. Martinez, *J. Comput. Chem.*, 2009, **30**, 2157-2164.
40 A. I. Jewett, Z. Y. Zhuang and J. E. Shea, *Biophys. J.*, 2013, **104**, 169A-169A.
41 M. A. Harris, T. R. Pearce, T. Pengo, H. Kuang, C. Forster and E. Kokkoli, *Nanomedicine: NBM*, 2018, **14**, 85-96.
42 A. M. Smith, M. Vinchurkar, N. Gronbech-Jensen and A. N. Parikh, *J. Am. Chem. Soc.*, 2010, **132**, 9320-9327.
43 A. West, K. Ma, J. L. Chung and J. T. Kindt, *J. Phys. Chem. A*, 2013, **117**, 7114-7123.
44 O. Regev, J. F. Gohy, B. G. G. Lohmeijer, S. K. Varshney, D. H. W. Hubert, P. M. Frederik and U. S. Schubert, *Colloid. Polym. Sci.*, 2004, **282**, 407-411.
45 M. M. Zetterberg, S. Ahlgren, V. A. Hernandez, N. Parveen and K. Edwards, *J. Colloid Interface Sci.*, 2016, **484**, 86-96.
46 S. A. Arnold, S. Albiez, A. Bieri, A. Syntychaki, R. Adaixo, R. A. McLeod, K. N. Goldie, H. Stahlberg and T. Braun, *J. Struct. Biol.*, 2017, **197**, 220-226.
47 S. E. Wilner, S. E. Sparks, D. Cowburn, M. E. Girvin and M. Levy, *J. Am. Chem. Soc.*, 2015, **137**, 2171-2174.
48 I. A. Pedroso, L. F. Duarte, G. Yanez, K. Burkewitz and T. M. Fletcher, *Biopolymers*, 2007, **87**, 74-84.
49 J. Kypr, I. Kejnovska, D. Renciuk and M. Vorlickova, *Nucleic Acids Res.*, 2009, **37**, 1713-1725.
50 E. W. Choi, L. V. Nayak and P. J. Bates, *Nucleic Acids Res.*, 2010, **38**, 1623-1635.
51 J. Mohanty, N. Barooah, V. Dhamodharan, S. Harikrishna, P. I. Pradeepkumar and A. C. Bhasikuttan, *J. Am. Chem. Soc.*, 2013, **135**, 367-376.
52 A. Renaud de la Faverie, A. Guedin, A. Bedrat, L. A. Yatsunyk and J.-L. Mergny, *Nucleic Acids Res.*, 2014, **42**, e65-e65.
53 S. Liu, P. Peng, H. Wang, L. Shi and T. Li, *Nucleic Acids Res.*, 2017, **45**, 12080–12089.
54 A. Singh, T. G. Burke, J. M. Calvert, J. H. Georger, B. Herendeen, R. R. Price, P. E. Schoen and P. Yager, *Chem. Phys. Lipids*, 1988, **47**, 135-148.
55 B. R. Ratna, S. Baraltosh, B. Kahn, J. M. Schnur and A. S. Rudolph, *Chem. Phys. Lipids*, 1992, **63**, 47-53.
56 B. N. Thomas, C. R. Safinya, R. J. Plano and N. A. Clark, *Science*, 1995, **267**, 1635-1638.
57 B. Yang, S. Kamiya, H. Yui, M. Masuda and T. Shimizu, *Chem. Lett.*, 2003, **32**, 1146-1147.
58 A. Singh, E. M. Wong and J. M. Schnur, *Langmuir*, 2003, **19**, 1888-1898.
59 M. S. Spector, A. Singh, P. B. Messersmith and J. M. Schnur, *Nano Lett.*, 2001, **1**, 375-378.
60 M. Masuda and T. Shimizu, *Langmuir*, 2004, **20**, 5969-5977.
61 J. P. K. Doye, T. E. Ouldridge, A. A. Louis, F. Romano, P. Sulc, C. Matek, B. E. K. Snodin, L. Rovigatti, J. S. Schreck, R. M. Harrison and W. P. J. Smith, *Phys. Chem. Chem. Phys.*, 2013, **15**, 20395-20414.
62 N. K. Li, H. S. Kim, J. A. Nash, M. Lim and Y. G. Yingling, *Mol. Simul.*, 2014, **40**, 777-783.
63 O.-S. Lee, S. I. Stupp and G. C. Schatz, *J. Am. Chem. Soc.*, 2011, **133**, 3677-3683.

64 I. W. Fu, C. B. Markegard, B. K. Chu and H. D. Nguyen, *Langmuir*, 2014, **30**, 7745-7754.
65 S. J. Marrink, H. J. Risselada, S. Yefimov, D. P. Tieleman and A. H. de Vries, *J. Phys. Chem. B*, 2007, **111**, 7812-7824.
66 R. Goetz and R. Lipowsky, *J. Chem. Phys.*, 1998, **108**, 7397-7409.
67 S. O. Nielsen, C. F. Lopez, G. Srinivas and M. L. Klein, *J. Phys.: Condens. Matter*, 2004, **16**, R481-R512.
68 J. C. Shelley, M. Y. Shelley, R. C. Reeder, S. Bandyopadhyay and M. L. Klein, *J. Phys. Chem. B*, 2001, **105**, 4464-4470.
69 R. D. Groot and K. L. Rabone, *Biophys. J.*, 2001, **81**, 725-736.
70 M. J. Stevens, *J. Chem. Phys.*, 2004, **121**, 11942-11948.
71 I. R. Cooke, K. Kremer and M. Deserno, *Phys. Rev. E*, 2005, **72**, 011506.
72 M. Muller, K. Katsov and M. Schick, *Phys. Rep.*, 2006, **434**, 113-176.
73 C. Y. Xing and R. Faller, *J. Phys. Chem. B*, 2008, **112**, 7086-7094.
74 T. E. Gartner, III and A. Jayaraman, *Macromolecules*, 2019, **52**, 755-786.
75 W. Humphrey, A. Dalke and K. Schulten, *J. Mol. Graphics Modell.*, 1996, **14**, 33-38.
76 S. E. Feller, *Curr. Opin. Colloid Interface Sci.*, 2000, **5**, 217-223.

The ssDNA secondary structure and tail length of ssDNA-amphiphiles are used to control the length and diameter of ssDNA nanotubes

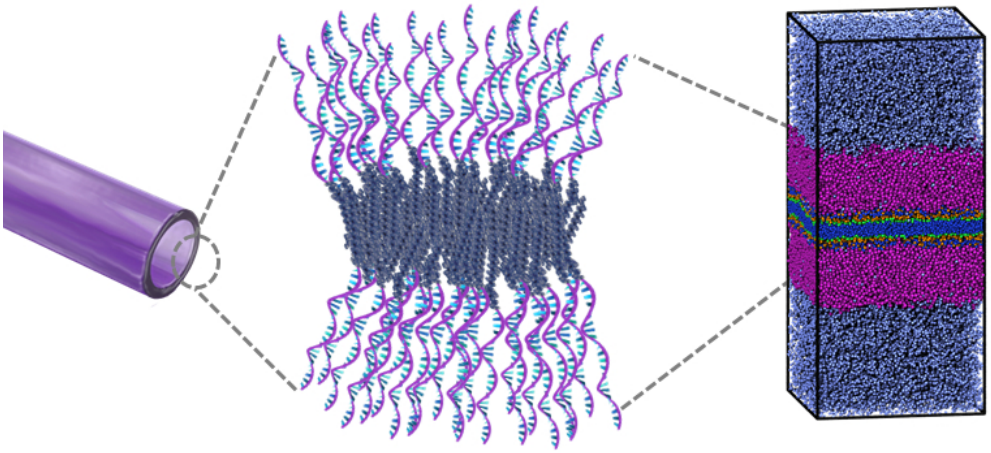

84x39mm (232 x 232 DPI)